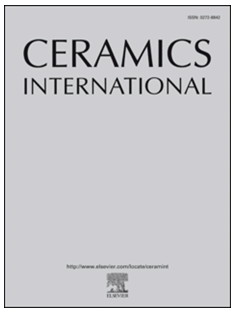

Efficient photocatalytic hydrogen production over titanate/titania nanostructures modified with nickel

Jasmina Dostanić, Davor Lončarević, Vladimir B. Pavlović, Jelena Papan, Jovan M. Nedeljković

PII: S0272-8842(19)31701-8

DOI: https://doi.org/10.1016/j.ceramint.2019.06.200

Reference: CERI 22009

To appear in: *Ceramics International*

Received Date: 22 April 2019

Revised Date: 18 June 2019

Accepted Date: 19 June 2019

Please cite this article as: J. Dostanić, D. Lončarević, V.B. Pavlović, J. Papan, J.M. Nedeljković, Efficient photocatalytic hydrogen production over titanate/titania nanostructures modified with nickel, *Ceramics International* (2019), doi: https://doi.org/10.1016/j.ceramint.2019.06.200.

Efficient photocatalytic hydrogen production over titanate/titania nanostructures modified with nickel

Jasmina Dostanić[a], Davor Lončarević[a], Vladimir B. Pavlović[b], Jelena Papan[c], Jovan M. Nedeljković[c]

[a]*Institute of Chemistry, Technology and Metallurgy, University of Belgrade (National Institute), Department of Catalysis and Chemical Engineering, Njegoševa 12, Belgrade, Republic of Serbia*

[b]*Faculty of Agriculture, University of Belgrade, Department of Agricultural Engineering, Nemanjina 6, 11080 Zemun, Republic of Serbia*

[c]*Institute of Nuclear Sciences Vinča, University of Belgrade, P.O. Box 522, 11001 Belgrade, Republic of Serbia*

ABSTRACT

Nickel-modified titanate/TiO_2 catalysts were prepared by deposition of nickel ions onto hydrothermally prepared titanate supports, followed by hydrogen temperature-programmed reduction. Two different nickel precursors (hydroxide and carbonate) were used to tune reducibility and to vary the crystal phase structure of the final catalysts. The precursor reducibility and functional properties of the final catalysts were investigated systematically using various characterisation techniques. The results revealed a more facile reduction of the hydroxide precursor compared to its carbonate counterpart. Moreover, it was found that the formation of the anatase phase was favoured by the use of the hydroxide precipitation agent. The photocatalytic activity towards hydrogen production of the prepared catalysts was evaluated in the presence of 2-propanol under simulated solar light irradiation. A thorough study of the photocatalytic performance of the synthesised catalysts was conducted as a function of the precipitation agent used and the reduction temperature applied. The catalyst with dominant anatase crystal phase displayed the highest photocatalytic activity with a maximum H_2 production rate of 1040 μmol h^{-1} g^{-1}, this being more than four times higher than that of its carbonate counterpart. The catalysts with titanate structure showed similar activity, independent of the precipitation method used. The nanotubular structure was found to be the dominant factor in the stability of photocatalysts under long-run working conditions.

Keywords: A. Powders: Chemical preparation; B. Nanocomposites; D. Titanium dioxide (TiO_2); Solar hydrogen production

1. INTRODUCTION

The increase in energy demand and the huge growth in fossil fuel consumption has raised serious environmental issues, such as loss of biodiversity, global warming, climate change, and air pollution. These undesired trends have urged extensive research activities directed towards the development of new, sustainable energy sources using green technologies. During the past decades, the interest in hydrogen as a fuel source has increased, due to its high gravimetric energy density, clean-burning qualities, the possibility of production from renewable sources, the possibility of delivering or storing a large amount of energy, *etc.* [1]. Currently, water-gas shift reactions and steam methane reforming are the common technologies of hydrogen production, whose main disincentives are high energy demand, large greenhouse gas emission and significant cost [2]. Over the last few years, photocatalytic hydrogen production via water splitting or alcohol reforming has been recognised as a promising approach for clean hydrogen energy generation [3–6]. Among the wide range of candidate photocatalysts [7, 8], TiO_2 has attracted the greatest interest, due to its suitable conduction and valence band alignment, low cost, nontoxicity, and stability against photo-corrosion [9, 10]. Given its favourable properties, numerous ongoing studies are directed towards the development of novel nanostructured titania-based materials, with well-controlled surface and morphological properties and improved photocatalytic efficiency, in order to achieve the desired level of practical efficiency [11].

One-dimensional (1-D) titanate nanomaterials have attracted considerable attention as potential photocatalysts, due to their favourable physicochemical properties (high specific surface area, narrow size distribution, small tube diameter, high surface charge density, fast ion diffusion, and enhanced light absorption) [12, 13]. Owing to their unique

morphology, as well as to excellent ion-exchange/intercalation activities, 1-D titanate materials have found application in various fields, such as catalysis, including photo-driven catalytic reactions, Li-ion batteries, dye-sensitised solar cells, *etc.* [11, 14]. In particular, titanate nanotubes (NTs) with a hollow structure have attracted special attention as catalysts, due to their high specific surface area (200–400 $m^2\ g^{-1}$), open mesoporous structure, nanometre-sized internal tube diameter (3–10 nm), and consequently large pore volume.

After the first successful synthesis of titanate nanotubes by Kasuga *et al.* [15, 16], the hydrothermal method has been widely used for the fabrication of 1-D titanate nanomaterials of various morphologies, such as nanotubes [17, 18], nanowires [19], nanofibers [20], and nanoribbons [21]. Although the preparation method is quite simple, every single step in its production, including choice of TiO_2 precursor [18, 22, 23], type and concentration of the alkaline solution [24], conditions of hydrothermal treatment [25–27], post-acid washing and thermal treatment [28] can significantly affect the structure and morphological features of the final titanate nanomaterial.

In order to be useful for hydrogen production via water splitting, a photocatalyst must possess a conduction band minimum that is more negative than the reduction potential of water [29]. Although TiO_2-based materials satisfy this essential criterion, they exhibit low efficiency for photocatalytic hydrogen production in their pristine form, due to fast electron–hole recombination and high overpotential for hydrogen production. To improve the hydrogen production efficiency, titania and titanate nanostructures have been modified by different approaches. The deposition of metal nanoparticles with high work function on the TiO_2 surface through photo-deposition, precipitation, or ion-exchange methods, has

proved to be an effective strategy in facilitating hydrogen evolution. Noble metals such as Pt [30, 31], Pd [32], Ag [33], and Au [34, 35], have been found to be efficient co-catalysts, with a reported hydrogen production rate as high as 20–40 mmol g^{-1} h^{-1} in alcohol/water systems. The enhanced activity of doped catalysts is related to the high work functions of the deposited metals (Pd 5.6 eV, Pt 5.7 eV, and Au 5.3–5.6 eV) and their abilities to form effective Schottky contacts with TiO_2 [36], thus increasing the charge separation in TiO_2 and, consequently, the number of charge carriers available for photoreactions.

Recently, efforts have been made to replace noble metal co-catalysts by less expensive and more abundant transition metals [37] and metal oxides [38, 39] that exhibit comparable or even, in some cases, superior activity compared to noble-metal-titania-based systems [40, 41]. Among them, nickel has been recognised as an excellent substitute for noble metals, due to its low cost, high abundance and high work function (5.3 eV) [36]. TiO_2 doped with nickel in various forms (NiO [42], metallic Ni [43, 44], $Ni(OH)_2$ [45], Ni/NiO core/shell structure [46]) has been the subject of recent studies dealing with hydrogen production from water/alcohol systems.

In the present study, Ni-modified titanate/titania catalysts were synthesised via different preparation routes. The activity and stability of synthesised catalysts towards photocatalytic hydrogen production were evaluated. The goal of our study was to understand better how variables such as functional properties of the support, mainly phase composition and textural and morphological features induced by thermal reduction treatment and precipitation method, contribute to the improvement of the activity and stability of the prepared catalysts.

2. EXPERIMENTAL

2.1. Materials

Nickel(II) nitrate hexahydrate, glycerol, sodium hydroxide, sodium carbonate, and 2-propanol were obtained from Alfa Aesar. All chemicals were of analytical grade quality and used without further purification. Commercially available TiO_2 was kindly supplied by Evonik Degussa GmbH (Aeroxide TiO_2 P25, 70% anatase 30% rutile, surface area 52 $m^2\ g^{-1}$, mean particle diameter approximately 30 nm).

2.2. Synthesis of hydrogen titanate nanotubes

Hydrogen titanate nanotubes (H-TiNTs) were prepared by hydrothermal reaction of commercial TiO_2 in NaOH solution, followed by ion-exchange with dilute HCl solution at room temperature, as described by Kasuga *et al.* [15]. The preparation was initiated by treating 2 g of the P25 TiO_2 powder with 250 mL of 10 M NaOH in a Teflon-lined autoclave at 150 °C for 24 h. The resulting sodium titanate precipitate was separated by filtration and then redispersed in 100 mL 0.1 M HCl under continuous stirring for 24 h in order to facilitate the ion-exchange reaction between sodium and hydrogen ions. The final product was separated by filtration and dried at 110 °C for 3 h.

2.3. Synthesis of Ni-modified titanate/titania catalysts

Titanate/titania catalysts modified with 1 wt % Ni were synthesised using a deposition/precipitation method. Briefly, 50 mg of $Ni(NO_3)_2 \cdot 6H_2O$ and 45 mg of glycerol were added to 20 mL of distilled water to form an aqueous nickel(II)–glycerol complex. Then, 1 g of H-TiNT was dispersed in this solution. Two sets of catalysts were prepared:

the first where the Ni complex was precipitated by dropwise addition of 0.5 M NaOH, and the second where 1.0 M Na_2CO_3 was used as a precipitation agent. The catalysts synthesised by the carbonate precipitation method were prepared without the addition of glycerol. The suspensions were stirred for 1 h, filtered by vacuum filtration and the obtained light green powders, $Ni(OH)_2$/TiNT (hydroxide precipitation method) and $Ni_2(OH)_2CO_3$/TiNT (carbonate precipitation method) were dried overnight at 70 ºC. Finally, titanate/titania catalysts modified with Ni were obtained by reduction of adsorbed Ni(II) species to the metallic form using temperature-programmed reduction process under H_2/Ar flow (5% of H_2 in H_2/Ar mixture, 20 mL min^{-1} flow rate) at different temperatures (400, 500, and 650 ºC) with a heating rate of 10 ºC min^{-1}. The catalysts prepared using NaOH as precipitating agent were labelled as NiT-x, while those prepared using Na_2CO_3 were labelled as NiTC-x, where x corresponds to the reduction temperature.

2.4. Characterisation of unmodified and Ni-modified titanate/titania catalysts

Hydrogen temperature-programmed reduction (TPR) profiles were obtained using Thermo Finningen TPRDO 1100 apparatus, equipped with a thermal conductivity detector (TCD) coupled to a MS detector (Thermo Star GSD320). Prior to the reduction, the sample (~50 mg) was pre-treated in flowing Ar stream at 110 °C for 60 min. Reduction profiles were obtained in the temperature range of 50 to 1000 ºC (heating rate of 10 ºC min^{-1}) under H_2/Ar flow (5% of H_2 in H_2/Ar mixture, 20 mL min^{-1} flow rate). The total amount of consumed hydrogen (μmol g^{-1}) was calculated by integrating the area under the obtained reduction peak. In addition, mass spectrometry signals at m/z 18, 28, and 44 were recorded to detect the masses of H_2O, CO, and CO_2 molecules, respectively.

The surface composition was determined by X-ray photoelectron spectroscopy (XPS) using a VG ESCALAB II electron spectrometer under a base pressure of 1×10^{-8} Pa. The photoelectron spectra were excited using un-monochromatised Al Kα radiation (hν = 1486.6 eV) with a total instrumental resolution of 1 eV. The C_{1s} line of adventitious carbon at 285 eV was used as an internal standard to calibrate the binding energies. The photoelectron spectra were corrected by subtracting a Shirley-type background and were quantified using the peak area and Scofield's photo-ionisation cross-sections.

The X-ray diffraction (XRD) powder patterns were recorded using a Rigaku SmartLab instrument under Cu $K\alpha_{1,2}$ radiation. The intensity of diffraction was measured with continuous scanning at 2° min^{-1}.

Transmission electron microscopy (TEM) images were obtained using a JEOL 2010F-FasTEM with an acceleration voltage of 200 kV. Samples were prepared by drop-casting an alcoholic solution of samples onto 200 mesh formvar carbon copper or lacey carbon copper grids.

Nitrogen adsorption–desorption isotherms were determined on a Sorptomatic 1990 Thermo Finnigan automatic system using nitrogen physisorption at –196 °C. Before measurement, the samples were degassed at 30 °C for 3 h. The specific surface area of the samples was calculated from the nitrogen adsorption–desorption isotherms according to the Brunauer, Emmett, and Teller (BET) method. Pore-size distributions were calculated from the desorption branch of the corresponding nitrogen isotherm, applying the Barrett, Joyner, and Halenda (BJH) method.

Optical properties of samples were studied in the wavelength range of 300 nm to 1.3 μm by diffuse reflectance spectroscopy measurements (Shimadzu UV-2600 UV-Vis spectrophotometer equipped with an integrated sphere ISR-2600 Plus).

2.5. Photocatalytic hydrogen production test

Photocatalytic hydrogen production over unmodified and Ni-modified catalysts was performed under simulated solar light irradiation in 2-propanol/water solution. Photocatalytic tests were carried out in the photocatalytic reactor (ACE glass), equipped with standard reaction flask, quartz immersion well and 100 W mercury lamp. The cooling of the reaction mixture to 25 ºC was performed using a JULABO F25 circulation thermostat. First, 125 mg of the sample was suspended in 250 mL of 2-propanol/water mixture (1.0 vol % of 2-propanol) and transferred to the reaction vessel. Oxygen was removed from suspension with Ar flow for 30 min, and prior to illumination the Ar flow was adjusted to 15 mL min^{-1}. During illumination, the effluent gas was analysed every 15 min by gas chromatography (Perkin Elmer F33 GC with a TCD) to quantify the production of H_2. A calibration curve was obtained by performing an analysis of samples with a known amount of H_2 in the H_2/Ar mixture.

3. RESULTS AND DISCUSSION

3.1. Formation mechanism and characterisation of Ni-modified titanate/titania catalysts

TPR/MS analysis was performed to study the reducibility of hydroxide and carbonate nickel precursors and to determine the type and amount of reducible species present in the

samples. Figure 1 shows that both precursors display broad asymmetric reduction profiles in the temperature range 180–900 ºC. In order to gain deeper insights into the reducible species, the obtained reduction profiles were deconvoluted into four peaks. The low-temperature peak, marked as a cross-hatched section, was attributed to the reduction of Ni(II) species. For the hydroxide precursor, the peak is centred at 450 ºC, while for the carbonate precursor the peak is centred at 500 ºC. It is essential to note that the reduction peak of the hydroxide precursor is shifted to lower temperature, indicating a more facile reduction of the hydroxide precursor compared to its carbonate counterpart. Although not being of central importance for this study, the peaks corresponding to the reduction of species other than Ni(II) were also identified [47, 48]. Briefly, the second peak, centred at ~540 ºC, can be attributed to the reverse water-gas shift reaction, leading to the formation of CO, as evidenced by mass spectroscopy. As expected, higher intensities of CO and CO_2 signals were obtained during the reduction of carbonate precursor. The remaining two high-temperature peaks were assigned to the dehydroxylation and consequent reduction of Ti^{4+} cations to Ti^{3+}, leading to the formation of oxygen vacancies [49].

Figure 1

Based on the observed TPR profiles, temperatures of 400, 500, and 650 ºC were chosen for the reduction of the nickel precursors. Temperatures of 500 and 650 ºC were suitable to ensure complete reduction of Ni(II) species, while 400 ºC was chosen as the predicted maximum temperature for maintaining the nanotubular structure.

Besides analysis of catalyst precursor reducibility, TPR was also used for catalyst preparation, through reduction of nickel species and calcination at a predetermined temperature. The amount of hydrogen consumed for the reduction of nickel precursors

(Ni(II)→Ni(0)) was calculated by integration of the peak area of the signal during the reduction, and the obtained data are summarised in Table 1. Taking into account the amount of hydrogen required for complete reduction of the Ni precursor and the experimentally determined amounts of hydrogen consumption, the content of reduced Ni-phase upon reduction process was determined.

Table 1

Inspection of the obtained values revealed a lower content of reduced nickel within samples reduced at 400 ºC (0.1 and 0.2 wt % for NiTC-400, and NiT-400, respectively). On the other hand, the temperatures of 500 and 650 ºC were found to be sufficient to ensure complete reduction of nickel species, resulting in samples (NiT-500, NiTC-500 and NiT-650) with metallic nickel content close to their theoretical value (1 wt %).

Figure 2a shows a typical XRD pattern of the starting material – unmodified titanate nanotubes (H-TiNTs) with main peaks at 24, 28, 43 and 48º. The exact structure of titanate nanotubes is still under debate. So far, multiple titania/titanate phases, including anatase TiO_2 [15], hydrated and non-hydrated analogous of monoclinic $H_2Ti_3O_7$ [50], monoclinic $H_2Ti_4O_9$ [51, 52] orthorhombic $H_2Ti_2O_5 \cdot H_2O$ [53], and lepidocrocite-type titanate $H_{0x}Ti_{2-x/4}v_{x/4}O_4$ (where $x \approx 0.7$ and v represents vacancy) [54, 55] have been proposed to represent the crystal structure of the nanotubes. The proposed crystal structures have some features in common: they consist of layers of (1 0 0) planes consisting of edge- and corner-sharing TiO_6 octahedra building up zigzag or flat layered structures with exchangeable hydrogen atoms situated between the layers [56]. A more detailed insight into the exact crystal structure of titanate nanotubes could be attained from the products obtained after thermal treatment [57]. Based on the results presented further below, we assigned the initial

nanotube structure to the monoclinic tetratitanate ($H_2Ti_4O_9 \cdot H_2O$) with lattice dimensions a = 1.877, b = 0.375, and c = 1.162 nm (JCPDS: 00-063-0655). Further, the characteristic diffraction peaks of anatase and rutile phases of starting TiO_2 P25 were not detected in XRD spectra, indicating complete transformation of the titania to hydrogen titanate structure after the hydrothermal treatment.

Figure 2

The TEM data of synthesised H-TiNTs revealed a multilayer tube-like structure with a length of several hundreds of nanometres, and external and inner diameters of 21 and 6.5 nm, respectively (Figure 3a and b). The distance between the adjacent layers was found to be 1.04 nm, somewhat greater in comparison to values reported in the literature [27, 58, 59].

Figure 3

According to EDX analysis, H-TiNTs consisted only of titanium and oxygen, indicating complete ion-exchange of the intercalated sodium ions by hydrogen ions (Figure S1a, Supporting Information). The elemental composition of unmodified H-TiNTs is shown in Table 1.

The synthesised H-TiNTs were characterised further by nitrogen adsorption–desorption isotherm (Figure 4a). According to IUPAC classification, the isotherm belongs to type IV, typical of mesoporous materials, with an H3 hysteresis loop, characteristic of aggregates or agglomerates of particles forming slit-shaped pores with non-uniform size and/or shape [60]. The BJH method was further employed to analyse the pore-size distributions, and the results are presented in Figure 4b. The obtained pore-size distribution curve, calculated from the desorption branch of the isotherm, shows an average pore

diameter of about 13 nm. The textural properties, including BET surface area, average pore size, and total pore volume are summarised in Table 1.

Figure 4

Ni-modified titania/titanate catalysts were obtained by reduction of $Ni(OH)_2$ and $Ni_2(OH)_2CO_3$ on H-TiNT supports at different temperatures (400, 500, and 650 ºC) and characterised using the same techniques as for unmodified H-TiNTs.

XRD patterns of NiT-400 and NiTC-400 are presented in Figure 2a. No significant differences between the XRD pattern of H-TNTs and catalysts synthesised at 400 ºC were observed. However, despite their coincident peak positions, the diffraction patterns of catalysts reduced at 400 ºC exhibited a strengthening of the peak at $2\theta \approx 28^o$ relative to that at $2\theta \approx 24^o$, which can be ascribed to the increase in the Na^+/H^+ ratio as a result of ion-exchange [61]. Considering that protons were not completely exchanged by sodium ions, the $Na_xH_{2-x}Ti_4O_9$ structure has been proposed for the titanate nanotubes calcined at 400 ºC. The absence of XRD peaks corresponding to metallic Ni suggests that its content was below the XRD detection limit.

The nitrogen adsorption–desorption isotherms of both catalysts prepared at 400 ºC belong to type IV in the IUPAC classification and show an H3 hysteresis loop, the same type as that obtained for the H-TiNT sample (Figure 4a). Both samples (NiT-400 and NiTC-400) had the same average pore diameter of about 15 nm, slightly larger than that determined for H-TiNTs (13 nm). The samples NiT-400 and NiTC-400 exhibited similar specific surface areas of 201 and 188 $m^2\ g^{-1}$, respectively. A small decrease in specific surface area compared to that determined for H-TiNTs (283 $m^2\ g^{-1}$) can be related to the loss of their microporous structure. However, the remaining high specific surface area,

almost unchanged pore diameter and mesoporous volume strongly indicate a non-collapsed nanotube structure for the samples thermally treated at 400 ºC.

Significant changes in crystal structure were observed upon thermal treatment at 500 ºC (Figure 2b). The XRD patterns of NiT-500 and NiTC-500 indicated the coexistence of two crystal phases (anatase and $Na_{0.8}Ti_4O_8$). The diffraction peaks at 25.1, 37.2, 47.9, 53.8, and 54.9º correspond to (1 0 1), (0 0 4), (2 0 0), (1 0 5), and (2 1 1) lattice planes of the anatase crystal phase, respectively. On the other hand, the diffraction peaks at 14.1, 15.0, 24.3, 28.7, 29.4, 32.7, 43.7, 44.4, and 47.3º belong to (0 1 –1), (1 –1 0), (1 2 2), (0 2 –2), (2 –1 –1), (0 2 3), (0 3 –3), (3 –2 –1), and (3 3 4) lattice planes of $Na_{0.8}Ti_4O_8$, respectively (JCPDS #73-1400). It should be noted that the XRD peaks of anatase and $Na_{0.8}Ti_4O_8$ are intense and sharp, indicating a good crystallinity of the samples reduced at 500 ºC. In addition, the XRD analysis of thermally treated samples provided valuable information concerning the structure of the starting H-TiNT. Since thermal treatment induced the formation of sodium tetratitanate ($Na_{0.8}Ti_4O_8$) phase, the orthorhombic hydrogen tetratitanate structure ($H_2Ti_4O_8 \cdot H_2O$) was assigned to initial titanate nanotubes.

The proposed explanation of phase transformation is as follows: Anatase phase is formed from hydrogen titanate during calcination at 500 ºC. Although a number of authors proposed that this phase transformation occurs through an intermediate metastable TiO_2(B) phase, this phase was not detected in XRD spectra [62–64]. According to the proposed mechanism [65], the appearance of TiO_2(B) phase depends on the morphology of the titanate nanostructure, which results in their different structural stability upon thermal treatment. Due to the weak structural stability of the nanotubes and their fast dehydration,

the transformation is either not occurring via intermediate TiO_2(B) phase or the intermediate TiO_2(B) phase is short-lived and therefore difficult to detect.

The second obtained phase, $Na_xH_{2-x}Ti_4O_8$, is thermally unstable and susceptible to phase transformation at temperatures above 400 ºC. The thermal treatment at 500 ºC leads to dehydration of interlayered –OH groups from the titanate nanostructure, while sodium ions remain intercalated between octahedral layers, directing the formation of $Na_{0.8}Ti_4O_8$ nanoribbons. The obtained results are consistent with the reported literature findings [66, 67].

The increase in the reduction temperature from 400 to 500 ºC also induced significant morphological changes. According to representative TEM images of NiT-500 (Figure 3c and d) and NiTC-500 (Figure 3e and f), calcination at 500 ºC led to deterioration of the nanotube morphology. The presented figures show the formation of a mixture of ribbon-like particles and particles with irregularly shaped morphology, decorated with nanosized metallic Ni particles (Figure 3c and e for NiT-500 and NiTC-500, respectively). The high-magnification TEM image (Figure 3d) reveals that the nanoribbons have basically a layered structure with a layer spacing of 0.596 nm.

EDX analysis confirmed the presence of sodium in NiT-500 and NiTC-500 samples, indicating that hydrogen ions were being partially replaced by sodium ions during the catalyst preparation (Figure S1b and c, Supporting Information). The average content of titanium and sodium elements in samples is presented in Table 1. It is established in the literature that the presence of sodium ions in the resulting titanate is an important stabilising factor that influences the phase transformation and morphology of the materials during thermal treatment [50, 57, 65].

Further transformation of the nanotube structure with calcination temperature was reflected through the observed variations in textural properties. It can be observed that an increase in temperature from 400 to 500 ºC was followed by changes in the profiles of the adsorption–desorption isotherms (Figure 4a). The NiT-500 and NiTC-500 catalysts display type IV isotherm with H1 hysteresis loops, characteristic of aggregates or agglomerates of spheroidal particles with uniform pore size and shape [60]. As a consequence, a significant decrease in specific surface area was observed for both samples. The loss of nanotubular morphology upon thermal treatment at 500 ºC led to the reduction of pore volume and an increase in average pore diameter (~70 nm) attributed to the inter-particle porosity (Figure 4b and Table 1).

The XPS analysis of NiT-500 and NiTC-500 samples was performed in order to obtain deeper insight into the electronic properties of the surface elements. The signals of Na, Ti, O, and Ni are present in the survey XPS spectra (Figure S2, Supporting Information). High-resolution XPS spectra of Ti, O, and Ni, shown in Figure 5, are almost identical for both samples. The characteristic peaks of Ti_{2p} at 458.3 and 464 eV (Figure 5a) were assigned to the tetravalent oxidation state of the titanium atom (Ti^{4+}). The absence of the $Ti_{2p3/2}$ feature at ~457 eV indicates that there was no formation of Ti^{3+} surface defects by reduction of Ti^{4+} under the applied reduction conditions. The core level O_{1s} peak is observed at 529.7 eV and was assigned to oxygen bound to the Ti^{4+} ions in the oxide lattice (Figure 5b). The oxidation state of the nickel species can be accessed from the binding energy of the $Ni_{2p3/2}$ electrons (852.6 eV and 853.7–854.9 eV for Ni(0) and Ni(II), respectively [68]). The high-resolution spectra of $Ni_{2p3/2}$ show the peak with binding energy of 855.5 eV with a broad satellite at 861 eV [69, 70] characteristic of Ni(II) and the low-

intensity peak at 852.1 eV characteristic of Ni(0) species (Figure 5c). The presence of surface Ni(II) species in NiT-500 and NiTC-500 samples is more likely the consequence of partial oxidation of metallic nickel during sample transfer before XPS measurement than of incomplete reduction under the applied experimental conditions.

Figure 5

To quantify the amount of NiO formed, we performed repeated TPR of already reduced samples, that were subsequently exposed to air for 1h, which simulates the conditions that actually occurred before the photocatalytic tests. The results revealed that the amount of hydrogen consumed for the reduction of these samples is ~20 % of the amount of hydrogen required for the complete reduction of the Ni precursors in non-reduced samples. It can be revealed that 20% of total metallic Ni amount was converted to NiO, after being exposed to air. The obtained results, joined with the results of XPS analysis, indicate the existence of core/shell structure model where core metal is coated by active thin NiO shell.

TEM results could give us indication that the size of metallic Ni particles is not larger than 30 nm, leading to the size of formed NiO layer of ~2 nm. Since metallic Ni is coated by 2 nm thick layer of NiO, the XPS spectra showed low-intensity peak characteristic for metallic Ni, while the main peak originated from NiO.

The increase in temperature to 650 ºC induced further changes in morphological, textural and structural properties. According to the obtained XRD patterns (Figure 2b), the increase in temperature to 650 ºC led to an increase in $Na_{0.8}Ti_4O_8$ phase content at the expense of anatase phase. This effect can be explained by enhanced dehydration of –OH groups at a higher temperature that promotes binding of intercalated sodium ions to TiO_6

octahedral structures in the titanate. The proposed mechanism is supported by EDAX measurements that indicate a higher Na/Ti ratio compared to that of samples reduced at 500 ºC (Table 1, Figure S1d, Supporting Information). The TEM analysis shows that the morphology of NiT-650 catalyst is similar to the morphology of NiT-500 and NiTC-500 samples with the additional deterioration of the nanotubular structure; a representative TEM image of NiT-650 is presented in Figure S3a and b in Supporting Information. The additional decrease in the specific surface area and reduction in pore volume was also observed after temperature increase to 650 ºC (Table 1).

3.2. Photocatalytic hydrogen production over titanate/titania catalysts modified with Ni

Photocatalytic hydrogen production efficiency of H-TiNTs and Ni-modified titanate/titania catalysts (NiT-400, NiTC-400, NiT-500, NiTC-500, and NiT-650) was evaluated under simulated sunlight irradiation in the presence of 2-propanol as a sacrificial agent. It is well known that 2-propanol can be easily oxidised by photogenerated holes, thus suppressing electron–hole recombination [71]. In addition, electron injection from the $(CH_3)_2\dot{C}OH$ radical to the conduction band of the titanate/titania nanostructure occurs due to the large negative potential of the $(CH_3)_2\dot{C}OH$ radical (–1.23 eV *versus* NHE [72]), doubling the yield of electrons. The performed preliminary tests demonstrated no appreciable H_2 production in the absence of either irradiation or photocatalyst, suggesting that the major H_2 production was driven by photocatalytic reaction.

Time-dependent rates of photocatalytic hydrogen production over the studied catalysts are presented in Figure 6. As evidenced from the obtained results the unmodified

H-TiNT exhibited low activity in hydrogen production. Although this reaction is thermodynamically possible, bearing in mind the relative positions of the conduction band of H-TiNT and the reduction potential of hydrogen, the catalyst showed negligible activity due to the high overpotential for H_2 evolution and fast electron–hole recombination rate. The observed low activities of H-TiNT are in accordance with the literature data, showing that hydrothermally synthesised titanate is inactive in photocatalytic hydrogen production [73] and in the degradation of organic pollutants [57, 74].

Figure 6

The presence of metallic nickel deposited on the surface of the synthesised catalysts dramatically improved efficiency of photocatalytic hydrogen production compared to the unmodified ones. Even the catalyst with a small content of metallic Ni (0.2 wt %), NiT-400, exhibited up to 10 times higher photocatalytic activity compared to unmodified ones. According to the conventional explanations, the metallic Ni lowers the overpotential for hydrogen evolution and suppresses electron–hole recombination, acting as an electron sink [75].

The results also revealed a significant difference in catalytic activity with variation of calcination temperature. The NiT-500 photocatalyst, prepared at a calcination temperature of 500 ºC from hydroxide precursor, exhibited the highest hydrogen production rate (1042 μmol h^{-1} g^{-1}). Despite the fact that NiT-500 has a significantly smaller specific surface area (53 m^2 g^{-1}) compared to NiT-400 (201 m^2 g^{-1}), the catalyst was found to exhibit 2.5 times higher hydrogen production activity (Table 2). This higher activity can be explained by the presence of a highly photocatalytically active anatase crystal phase that exceeds the activity of the less active titanate structure, as well as improved crystallinity.

Similar observations have been reported by other studies, which found the increased photocatalytic performance of titanate nanotubes invoked by crystal phase transformation [76]. Additionally, the influence of a higher content of deposited Ni (1.0 wt %) and improved light harvesting ability due to absorption in the visible and near infra-red spectral region (Figure S4, Supporting Information) on the photocatalytic efficiency of NiT-500 cannot be ruled out.

Table 2

A further increase in reduction temperature led to decreased catalytic activity. The modest hydrogen production activity of the NiT-650 catalyst was caused by the transformation of active anatase phase to sodium titanate phase, i.e., a loss of anatase structure (Figure 2b), pore structure deterioration (Figure 4b) and consequently decreased available BET surface area (Table 1).

A strong effect of precursor type, i.e., the precipitation agent used, on the characteristics of the prepared catalysts is reflected through pronounced differences in their photocatalytic activities (Figure 6). As evidenced by the results obtained, the samples prepared at 400 ºC (NiT-400 and NiTC-400) exhibited similar photocatalytic activity at longer irradiation times (>1 h). The samples displayed lower activity than NiT-500, but higher than NiTC-500. The observed higher hydrogen production rates of NiT-400 and NiTC-400 samples compared to NiTC-500 can be explained by their significantly larger specific surfaces (201 and 188 m^2 g^{-1}, respectively). However, the importance of the anatase phase in the photocatalytic process can be discerned from the maximal hydrogen production rates normalised to the specific surface area (Table 2). For example, this value is

over 2.5 times higher for NiTC-500 (6.74 μmol h^{-1} m^{-2}) than the corresponding values obtained for NiT-400 and NiTC-400 catalysts (2.01 and 2.66 μmol h^{-1} m^{-2}).

On the other hand, clear differences in photoactivity between the catalysts reduced at 500 ºC were observed. The sample prepared from hydroxide precursor (NiT-500) exhibited remarkably higher activity compared to its carbonate counterpart (NiTC-500). The better performance of NiT-500 cannot fully be explained by its higher specific surface area. As evidenced from Table 2, maximal hydrogen production rate normalised to the specific surface area is higher for hydroxide-origin catalysts, suggesting that additional catalyst properties, other than surface area, have a prominent effect on catalyst performance. According to the obtained XRD patterns (Figure 2b), NiT-500 catalyst contains a higher amount of anatase phase compared to its carbonate counterpart, NiTC-500, implying the dominance of anatase phase in determining catalyst performance.

In the context of photocatalytic water splitting applications, long-term catalyst stability is an important milestone for achieving high hydrogen production efficiency and long-term performance. For the purpose of studying catalyst stability through a continuous reaction system, it is more appropriate to gain information about catalyst stability from performed activity tests than to perform additional recycling tests.

The results presented in Figure 6 indicate that upon reaching the maximum rate ($t \approx 40$ min), the hydrogen production rate fell over varying times, depending on the applied catalyst. Since photocatalytic hydrogen production is carried out through a continuous reaction system, a stable catalyst is expected to exhibit a constant rate of hydrogen production whereas any perceivable change in hydrogen production after reaching the steady-state reflects a reduction in catalyst activity. In the context of this study,

the hydrogen production rate, R (μmol h^{-1} g^{-1}) is normalised to the maximal hydrogen production rate, R_{max} (μmol h^{-1} g^{-1}) (Figure 7a) to quantify the activity drop. The most scientifically sound methodology for comparison of catalyst stability involves comparing the performance of catalysts at equal conversion levels rather than reaction times. Therefore, the reduction in catalyst activities was compared for the same amount of hydrogen evolved. In the next step, the cumulative hydrogen evolution curves (Figure 7b) were generated by integrating the curves in Figure 6. It should be noted that after dead time of 40 min, an almost linear dependence of evolved hydrogen versus time exists for all catalysts. For the sake of clarity, only two values of evolved hydrogen were selected (0.5 mmol g^{-1} and 1.0 mmol g^{-1}) and the required time for their production was determined. The obtained values of production times have been used further to read off the values of R/R_{max} from Figure 7a. The stability of the catalysts NiT-400, NiTC-400, NiT-500, and NiTC-500, defined as the ratio between hydrogen production rate observed at the reaction time when predetermined production of hydrogen is achieved (R_t) and maximal hydrogen production rate (R_{max}), is presented in Figure 7c. The unmodified H-TiNT and NiT-650 were discarded from further analysis due to the low hydrogen production yield.

Figure 7

The obtained results revealed that the catalyst stability is strongly influenced by the catalyst preparation temperature; the catalysts reduced at 400 ºC exhibited higher stability compared to the stability of those reduced at 500 ºC. Furthermore, carbonate-origin catalysts showed lower stability compared to their hydroxide counterparts. Thus, the greatest drop in activity was observed for NiTC-500, while NiT-400 possessed the highest stability among the investigated samples. The observed results undoubtedly indicate the

importance of preservation of the nanotubular structure for increased stability of the catalysts after thermal treatment.

CONCLUSIONS

Nickel-modified catalysts were prepared by deposition/precipitation of nickel ions onto titanate supports using hydroxide or carbonate precipitation agents, followed by hydrogen temperature-programmed reduction. The temperatures of 500 and 650 ºC were found to be suitable reduction temperatures to ensure complete reduction of Ni(II) species, while 400 ºC was the maximum temperature for maintaining their nanotubular structure. The nickel hydroxide precursor showed more facile reducibility compared to its carbonate counterpart. The catalysts preserved a mesoporous titanate structure with nanotube morphology up to 400 ºC, with high specific surface area and unchanged pore diameter. The increase in temperature above 400 ºC resulted in deterioration of nanotubular morphology with a significant reduction in specific surface area, loss of mesoporous structure and transformation of titanate into anatase and sodium titanate phases. The catalyst reduced at 500 ºC using hydroxide precipitating agent displayed the highest photocatalytic activity towards hydrogen production. The better performance of the hydroxide catalyst compared to its carbonate counterpart was attributed to its higher specific surface area and higher content of anatase phase. On the other hand, both carbonate and hydroxide catalysts reduced at 400 ºC, with high surface area and titanate phase structure, displayed similar photoactivity. The trade-off between the specific surface area and the presence of the anatase phase governs the optimisation of synthetic parameters that lead to an efficient photocatalyst for hydrogen production. The catalysts reduced at 400 ºC

displayed higher stability compared to those reduced at 500 ºC, highlighting the prominent influence of the retention of a nanotubular structure on catalyst stability.

Acknowledgements: This work was supported by the Ministry of Education, Science and Technological Development of the Republic of Serbia [Projects 45001, 45020, and 172057]. The authors thank Dr. Plamen Stefanov from the Bulgarian Academy of Sciences, Institute of General and Inorganic Chemistry, Sofia, Bulgaria for help in XPS analysis.

References

[1] S.A. Wells, A. Sartbaeva, V.L. Kuznetsov, P.P. Edwards, Hydrogen Economy, in: Encyclopedia of Inorganic and Bioinorganic Chemistry, John Wiley & Sons, Ltd, Hoboken, New Jersey, 2011.

[2] L.Z. Luling, L.J. Fan, A modified process for overcoming the drawbacks of conventional steam methane reforming for hydrogen production: Thermodynamic investigation, Chem. Eng. Res. Des. 104 (2015) 792–806.

[3] National Research Council and National Academy of Engineering, The Hydrogen Economy: Opportunities, Costs, Barriers, and R&D Needs, The National Academies Press. Washington, DC, 2004. https://doi.org/10.17226/10922.

[4] K. Shimura, H. Yoshida, Heterogeneous photocatalytic hydrogen production from water and biomass derivatives, Energy Environ. Sci. 4 (2011) 2467–2481.

[5] R. Abe, Recent progress on photocatalytic and photoelectrochemical water splitting under visible light irradiation, J. Photochem. Photobiol., C 11 (2010) 179–209.

[6] A. Fujishima, K. Honda, Electrochemical photolysis of water at a semiconductor electrode, Nature 238 (1972) 37–38.

[7] A. Kudo, Y. Miseki, Heterogeneous photocatalyst materials for water splitting, Chem. Soc. Rev. 38 (2009) 253–278.

[8] X. Chen, S. Shen, L. Guo, S.S. Mao, Semiconductor-based photocatalytic hydrogen generation, Chem. Rev. 110 (2010) 6503–6570.

[9] M.R. Hoffmann, S.T. Martin, W. Choi, D.W. Bahnemann, Environmental applications of semiconductor photocatalysis, Chem. Rev. 95 (1995) 69–96.

[10] N.R. Khalid, A. Majid, M. Bilal Tahir, N.A. Niaz, S. Khalid, Carbonaceous-TiO_2 nanomaterials for photocatalytic degradation of pollutants: A review, Ceram. Int. 43 (2017) 14552–14571.

[11] Y. Zhang, Z. Jiang, J. Huang, L.Y. Lim, W. Li, J. Deng, D. Gong, Y. Tang, Y. Lai, Z. Chen, Titanate and titania nanostructured materials for environmental and energy applications: A Review, RSC Adv. 5 (2015) 79479–79510.

[12] N. Liu, X. Chen, J. Zhang, J.W. Schwank, A review on TiO_2-based nanotubes synthesized via hydrothermal method: Formation mechanism, structure modification, and photocatalytic applications, Catal. Today 225 (2014) 34–51.

[13] Y.L. Pang, S. Lim, H.C. Ong, W.T. Chong, A critical review on the recent progress of synthesizing techniques and fabrication of TiO_2-based nanotubes photocatalysts, Appl. Catal., A 481 (2014) 127–142.

[14] L. Lin, X. Huang, L. Wang, A. Tang, Synthesis, characterization and the electrocatalytic application of prussian blue/titanate nanotubes nanocomposite, Solid State Sci. 12 (2010) 1764–1769.

[15] T. Kasuga, M. Hiramatsu, A. Hoson, T. Sekino, K. Niihara, Formation of titanium oxide nanotube, Langmuir 14 (1998) 3160–3163.

[16] T. Kasuga, M. Hiramatsu, A. Hoson, T. Sekino, K. Niihara, Titania nanotubes prepared by chemical processing, Adv. Mater. 11 (1999) 1307–1311.

[17] A.L. Papa, N. Millot, L. Saviot, R. Chassagnon, O. Heintz, Effect of reaction parameters on composition and morphology of titanate nanomaterials, J. Phys. Chem. C 113 (2009) 12682–12689.

[18] E. Morgado Jr., M.A.S. De Abreu, G.T. Moure, B.A. Marinkovic, P.M. Jardim, A.S. Araujo, Effects of thermal treatment of nanostructured trititanates on their crystallographic and textural properties, Mater. Res. Bull. 42 (2007) 1748–1760.

[19] J. Huang, Y. Cao, Z. Deng, H. Tong, Formation of titanate nanostructures under different NaOH concentration and their application in wastewater treatment, J. Solid State Chem. 184 (2011) 712–719.

[20] H.-K. Seo, G.-S. Kim, S.G. Ansari, Y.-S. Kim, H.-S. Shin, K.-H. Shim, E.-K. Suh, A study on the structure/phase transformation of titanate nanotubes synthesized at various hydrothermal temperatures, Sol. Energy Mater. Sol. Cells 92 (2008) 1533–1539.

[21] H.-H. Ou, S.-L. Lo, Review of titania nanotubes synthesized via the hydrothermal treatment: Fabrication, modification, and application, Sep. Purif. Technol. 58 (2007) 179–191.

[22] Y. Lan, X.P. Gao, H.Y. Zhu, Z.F. Zheng, T.Y. Yan, F. Wu, S.P. Ringer, D.Y. Song, Titanate nanotubes and nanorods prepared from rutile powder, Adv. Funct. Mater. 15 (2005) 1310–1318.

[23] D.L. Morgan, G. Triani, M.G. Blackford, N.A. Raftery, R.L. Frost, E.R. Waclawik, Alkaline hydrothermal kinetics in titanate nanostructure formation, J. Mater. Sci. 46 (2011) 548–557.

[24] L.M. Sikhwivhilu, S.S. Ray, N.J. Coville, Influence of bases on hydrothermal synthesis of titanate nanostructures, Appl. Phys. A: Mater. Sci. Process. 94 (2009) 963–973.

[25] D.L. Morgan, H.Y. Zhu, R.L. Frost, E.R. Waclawik, Determination of a morphological phase diagram of titania/titanate nanostructures from alkaline hydrothermal treatment of Degussa P25, Chem. Mater. 20 (2008) 3800–3802.

[26] D.V. Bavykin, B.A. Cressey, M.E. Light, F.C. Walsh, An aqueous, alkaline route to titanate nanotubes under atmospheric pressure conditions, Nanotechnology 19 (2008) 275604.

[27] D.V. Bavykin, V.N. Parmon, A.A. Lapkin, F.C. Walsh, The effect of hydrothermal conditions on the mesoporous structure of TiO_2 nanotubes, J. Mater. Science 14 (2004) 3370–3377.

[28] A. Turki, H. Kochkar, C. Guillard, G. Berhault, A. Ghorbel, Effect of Na content and thermal treatment of titanate nanotubes on the photocatalytic degradation of formic acid, Appl. Catal. B 138/139 (2013) 401–415.

[29] A.A. Ismail, D.W. Bahnemann, Photochemical splitting of water for hydrogen production by photocatalysis: A review, Sol. Energy Mater. Sol. Cells 128 (2014) 85–101.

[30] A. Naldoni, M. D'Arienzo, M. Altomare, M. Marelli, R. Scotti, F. Morazzoni, E. Selli, V. Dal Santoa, Pt and Au/TiO_2 photocatalysts for methanol reforming: Role of metal

nanoparticles in tuning charge trapping properties and photoefficiency, Appl. Catal. B 130–131 (2013) 239–248.

[31] Z.H.N. Al-Azri, V. Jovic, W.-T. Chen, D. Sun-Waterhouse, J.B. Metson, G.I.N. Waterhouse, Performance evaluation of Pd/TiO_2 and Pt/TiO_2 photocatalysts for hydrogen production from ethanol-water mixtures, Int. J. Nanotechnol. 11 (2014) 695–703.

[32] W. Jonesa, D.J. Martin, A. Caravaca, A.M. Beale, M. Bowker, T. Maschmeyer, G. Hartley, A. Masters, A comparison of photocatalytic reforming reactions of methanol and triethanolamine with Pd supported on titania and graphitic carbon nitride, Appl. Catal. B 240 (2019) 373–379.

[33] N.R. Khalid, E. Ahmed, M. Ahmad, N.A. Niaz, M. Ramzan, M. Shakil, T. Iqbal, A. Majid, Microwave-assisted synthesis of Ag–TiO_2/graphene composite for hydrogen production under visible light irradiation, Ceram. Int.42 (2016) 18257–18263.

[34] A.G. Dosado, W.-T. Chen, A. Chan, D. Sun-Waterhouse, G.I.N. Waterhouse, Novel Au/TiO_2 photocatalysts for hydrogen production in alcohol–water mixtures based on hydrogen titanate nanotube precursors, J. Catal. 330 (2015) 238–254.

[35] V. Jovic, W.-T. Chen, D. Sun-Waterhouse, M.G. Blackford, H. Idriss, G.I.N. Waterhouse, Effect of gold loading and TiO_2 support composition on the activity of Au/TiO_2 photocatalysts for H_2 production from ethanol–water mixtures, J. Catal. 305 (2013) 307–317.

[36] H.L. Skriver, N. Rosengaard, Surface energy and work function of elemental metals, Phys. Rev. B 46 (1992) 7157–7168.

[37] J. Ran, J. Zhang, J. Yu, M. Jaroniec, S.Z. Qiao, Earth-abundant cocatalysts for semiconductor based photocatalytic water splitting, Chem. Soc. Rev. 43 (2014) 7787–7812.

[38] K. Lalitha, G. Sadanandam, V.D. Kumari, M. Subrahmanyam, B. Sreedhar, N.Y. Hebalkar, Highly stabilized and finely dispersed Cu_2O/TiO_2: A promising visible sensitive photocatalyst for continuous production of hydrogen from glycerol:water mixtures, J. Phys. Chem. C, 114 (2010) 22181–22189.

[39] G. Sadanandam, K. Lalitha, V.D. Kumari, M.V. Shankar, M. Subrahmanyam, Cobalt doped TiO_2: A stable and efficient photocatalyst for continuous hydrogen production from glycerol: Water mixtures under solar light irradiation, Int. J. Hydrogen Energ. 38 (2013) 9655–9664.

[40] D.P. Kumar, M.V. Shankar, M.M. Kumari, G. Sadanandam, B. Srinivas, V. Durgakumari, Nano-size effects on CuO/TiO_2 catalysts for highly efficient H_2 production under solar light irradiation, Chem. Commun. 49 (2013) 9443–9445.

[41] S. Xu, A.J. Du, J. Liu, J. Ng, D.D. Sun, Highly efficient CuO incorporated TiO_2 nanotube photocatalyst for hydrogen production from water, Int. J. Hydrogen Energ. 36 (2011) 6560–6568.

[42] E.P. Melián, M.N. Suárez, T. Jardiel, J.M. Dona Rodríguez, A.C. Caballero, J. Arana, D.G. Calatayud, O. González Díaz, Influence of nickel in the hydrogen production activity of TiO_2, Appl. Catal. B 152–153 (2014) 192–201.

[43] W.-T. Chen, A. Chan, D. Sun-Waterhouse, T. Moriga, H. Idriss, G.I.N. Waterhouse, Ni/TiO_2: A promising low-cost photocatalytic system for solar H_2 production from ethanol–water mixtures, J. Catal. 326 (2015) 43–53.

[44] S. Peng, X. Zeng, Y. Li, Titanate nanotube modified with different nickel precursors for enhanced Eosin Y-sensitized photocatalytic hydrogen evolution, Int. J. Hydrogen Energ. 40 (2015) 6038–6049.

[45] J. Yu, Y. Hai, B. Cheng, Enhanced Photocatalytic H_2-Production Activity of TiO_2 by $Ni(OH)_2$ Cluster Modification, J. Phys. Chem. C 115 (2011) 4953–4958.

[46] E. Cui, G. Lu, Enhanced surface electron transfer by fabricating a core/shell Ni@NiO cluster on TiO_2 and its role on high efficient hydrogen generation under visible light irradiation, Int. J. Hydrogen Energ. 39 (2014) 8959–8968.

[47] M. Jablonska, TPR study and catalytic performance of noble metals modified Al_2O_3, TiO_2 and ZrO_2 for low-temperature NH_3-SCO, Catal. Commun. 70 (2015) 66–71.

[48] S. Zhang, Y. Guo, X. Li, X. Wu, Z. Li, The double peaks and symmetric path phenomena in the catalytic activity of Pd/Al_2O_3-TiO_2 catalysts with different TiO_2 contents, J. Solid State Chem. 262 (2018) 335–342.

[49] S. Chen, D. Li, Y. Liu, W. Huang, Morphology-dependent defect structures and photocatalytic performance of hydrogenated anatase TiO_2 nanocrystals, J. Catal. 341 (2016) 126–135.

[50] E. Morgado Jr., M.A.S. De Abreu, O.R. Pravia, B.A. Marinkovic, P.M. Jardim, F.C. Rizzo, A.S. Araújo, A study on the structure and thermal stability of titanate nanotubes as a function of sodium content, Solid State Sci. 8 (2006) 888–900.

[51] A. Nakahira, W. Kato, M. Tamai, T. Isshiki, K. Nishio, Synthesis of nanotube from a layered $H_2Ti_4O_9 \cdot H_2O$ in a hydrothermal treatment using various titania sources, J. Mater. Sci. 39 (2004) 4239–4245.

[52] S. Nosheen, F.S. Galasso, S.L. Suib, Role of Ti−O bonds in phase transitions of TiO_2, Langmuir 25 (2009) 7623–7630.

[53] C.-C. Tsai, H. Teng, Nanotube formation from a sodium titanate powder via low-temperature acid treatment, Langmuir 24 (2008) 3434–3438.

[54] T. Gao, H. Fjellvåg, P. Norby, Crystal Structures of Titanate Nanotubes: A Raman Scattering Study, Inorg. Chem. 48 (2009) 1423−1432.

[55] R. Ma, K. Fukuda, T. Sasaki, M. Osada, Y. Bando, Structural features of titanate nanotubes/nanobelts revealed by raman, X-ray absorption fine structure and electron diffraction characterizations, J. Phys. Chem. B 109 (2005) 6210–6214.

[56] Q. Chen, L.-M. Peng, Structure and applications of titanate and related nanostructures, Int. J. Nanotechnol. 4 (2007) 44–65.

[57] M. Qamar, C.R. Yoon, H.J. Oh, N.H. Lee, K. Park, D.H. Kim, K.S. Lee, W.J. Lee, S.J. Kim, Preparation and photocatalytic activity of nanotubes obtained from titanium dioxide, Catal. Today 131 (2008) 3–14

[58] Y.Q. Wang, G.Q. Hu, X.F. Duan, H.L. Sun, Q.K. Xue, Microstructure and formation mechanism of titanium dioxide nanotubes, Chem. Phys. Lett. 365 (2002) 427–431.

[59] F. Sallem, R. Chassagnon, A. Megriche, M. El Maaoui, N. Millot, Effect of mechanical stirring and temperature on dynamic hydrothermal synthesis of titanate nanotubes, J. Alloys Compd. 722 (2017) 785–796.

[60] G. Leofanti, M. Padovan, G. Tozzola, B. Venturelli, Surface area and pore texture of catalysts, Catal. Today 41 (1998) 207–219.

[61] A. Sandoval, C. Hernández-Ventura, Tatiana E. Klimova, Titanate nanotubes for removal of methylene blue dye by combined adsorption and photocatalysis, Fuel 198 (2017) 22–30.

[62] E. Morgado Jr, P.M. Jardim, B.A. Marinkovic, F.C. Rizzo, M.A.S. De Abreu, J.L. Zotin, A.S. Araújo, Multistep structural transition of hydrogentrititanate nanotubes into

TiO_2-B nanotubes: A comparison study between nanostructured and bulk materials, Nanotechnology 18 (2007) 495710–495719.

[63] G. Armstrong, A.R. Armstrong, J. Canales, P.G. Bruce Nanotubes with the TiO_2-B structure, Chem. Commun. 19 (2005) 2454–2456.

[64] D.V. Bavykin, M. Carravetta, A.N. Kulak, F.C. Walsh, Application of magic-angle spinning NMR to examine the nature of protons in titanate nanotubes, Chem. Mater. 22 (2010) 2458–2465.

[65] K. Kiatkittipong, Synthesis of Titania/Titanate Nanostructures for Photocatalytic Applications, A thesis submitted to The University of New South Wales, School of Chemical Engineering, The University of New South Wales (July 2012).

[66] X. Luan, Y. Wang, Thermal annealing and graphene modification of exfoliated hydrogen titanate nanosheets for enhanced lithium-ion intercalation properties, J. Mater. Sci. Technol. 30 (2014) 839–846.

[67] M. Zhang, Z. Jin, J. Zhang, X. Guo, J. Yang, W. Li, X. Wang, Z. Zhang, Effect of annealing temperature on morphology, structure and photocatalytic behavior of nanotubed $H_2Ti_2O_4(OH)_2$, J. Mol. Catal.A: Chem. 217 (2004) 203–210.

[68] M.C. Biesinger, B.P. Payne, L.W.M Lau, A. Gerson, R.S.C. Smart, X-ray photoelectron spectroscopic chemical state quantification of mixed nickel metal, oxide and hydroxide systems. Surf. Interface Anal. 41 (2009) 324–332.

[69] P. Girault, J.L. Grosseau-Poussard, J.F. Dinhut, L. Marechal, Influence of a chromium ion implantation on the passive behaviour of nickel in artificial sea-water, Nucl. Instrum. Methods Phys. Res. Sect. B 174 (2001) 439–452.

[70] A.P. Grosvenor, M.C. Biesinger, R.St.C. Smart, N.S. McIntyre, New interpretations of XPS spectra of nickel metal and oxides, Surf. Sci. 600 (2006) 1771–1779.

[71] C.R. López, E.P. Melián, J.A.O. Méndez, D.E. Santiago, J.M.D. Rodríguez, O. González Díaz, Comparative study of alcohols as sacrificial agents in H_2 production by heterogeneous photocatalysis using Pt/TiO_2 catalysts, J. Photochem. Photobiol., A 312 (2015) 45–54.

[72] M. Breitenkamp, A. Henglein, J. Lilie, Mechanism of the reduction of lead ions in aqueous solution (a pulse radiolysis study), Ber. Bunsenges. Phys. Chem. 80 (1976) 973–979.

[73] P. Wang, X. Yi, Y. Lu, H. Yu, J. Yu, *In-situ* synthesis of amorphous H_2TiO_3-modified TiO_2 and its improved photocatalytic H_2-evolution performance, J. Colloid Interf. Sci. 532 (2018) 272–279.

[74] S. Mozia, Application of temperature modified titanate nanotubes for removal of an azo dye from water in a hybrid photocatalysis-MD process, Catal. Today 156 (2010) 198–207.

[75] A.L. Luna, E. Novoseltceva, E. Louarn, P. Beaunier, E. Kowalska, B. Ohtani, M.A. Valenzuela, H. Remita, C. Colbeau-Justin, Synergetic effect of Ni and Au nanoparticles synthesized on titania particles for efficient photocatalytic hydrogen production, Appl. Catal. B 191 (2016) 18–28.

[76] B. Erjavec, R. Kaplan, A. Pintar, Effects of heat and peroxide treatment-on photocatalytic-activity of titanate nanotubes, Catal. Today 241 (2015) 15–24.

Figure Captions

Figure 1. TPR/MS profiles of **(a)** hydroxide and **(b)** carbonate precursors; reduction conditions: 5 vol % of H_2 in H_2/Ar mixture; flow rate 20 mL min^{-1}; heating rate 10 ºC min^{-1}.

Figure 2. Powder XRD patterns of **(a)** H-TiNT, NiT-400 and NiTC-400 and **(b)** NiT-500, NiTC-500 and NiT-650. Symbols indicate the observed possible reflections.

Figure 3. Low- and high-magnification TEM images of **(a, b)** H-TiNT**, (c, d)** NiT-500 and **(e, f)** NiTC-500.

Figure 4. (a) Nitrogen adsorption–desorption isotherms and **(b)** BJH pore-size distributions of the H-TiNT and series of synthesised Ni-modified titanate/titania catalysts.

Figure 5. High-resolution XPS spectra of **(a)** Ti_{2p}**, (b)** O_{1s} and **(c)** Ni_{2p} of synthesised NiT-500 and NiTC-500.

Figure 6. Time-dependent hydrogen evolution rates over H-TiNT and series of synthesised Ni-modified titanate/titania catalysts. Experimental conditions: temperature 25 ºC; concentration of catalysts 0.5 mg mL^{-1}; concentration of 2-propanol 1.0 vol %.

Figure 7. (a) Time-dependent photocatalytic hydrogen production rate (R) normalised to the maximal hydrogen production rate (R_{max}), **(b)** Cumulative hydrogen evolution curves, **(c)** The ratio between hydrogen production rates observed at the reaction time when 0.5 and 1.0 mmol g^{-1} production of hydrogen was achieved (R_t) and maximal hydrogen production rate (R_{max}).

Figure 1.

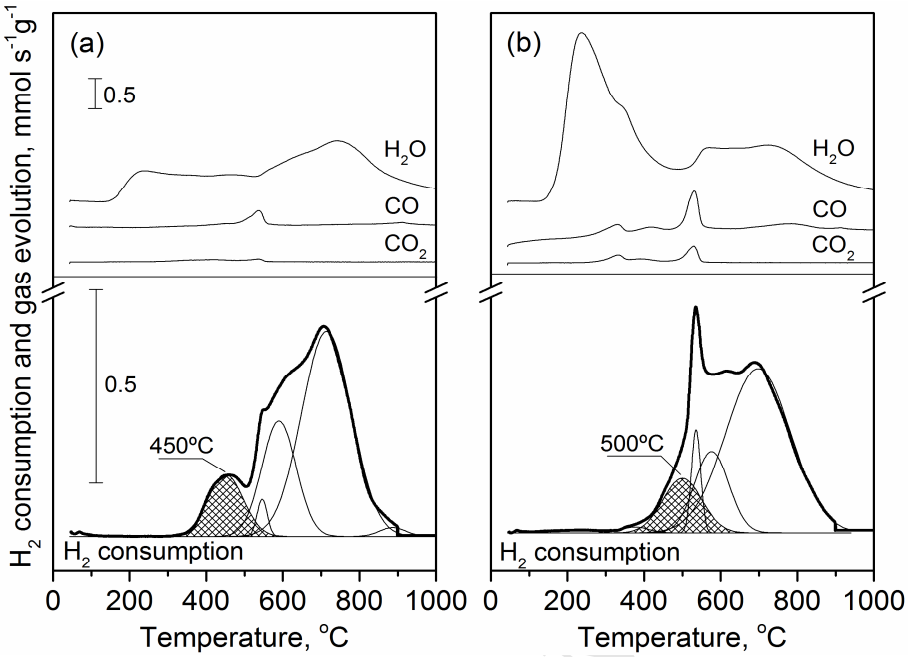

Figure 2.

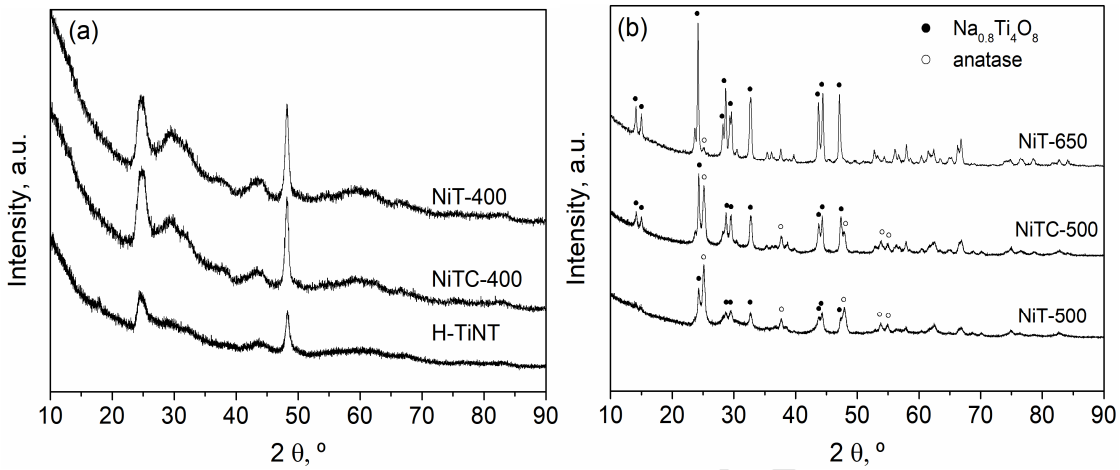

Figure 3.

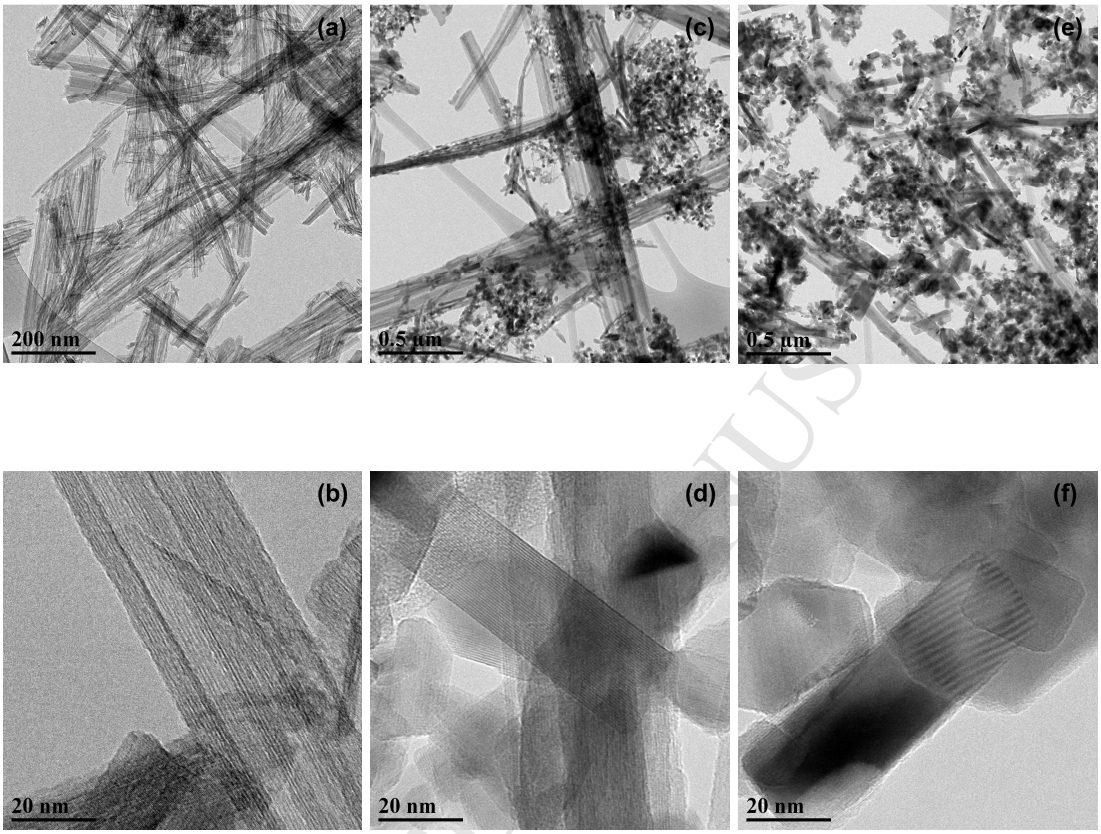

Figure 4.

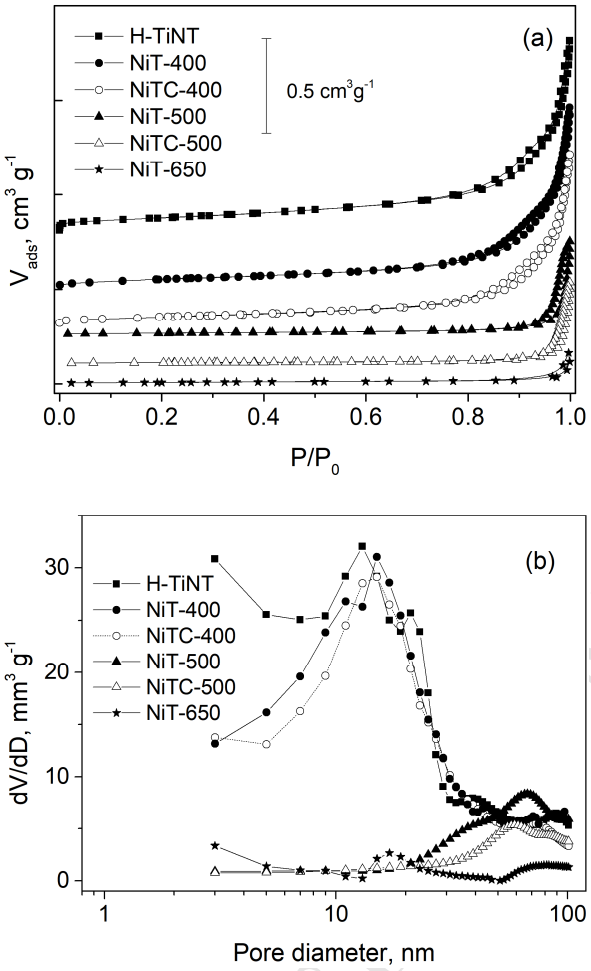

Figure 5.

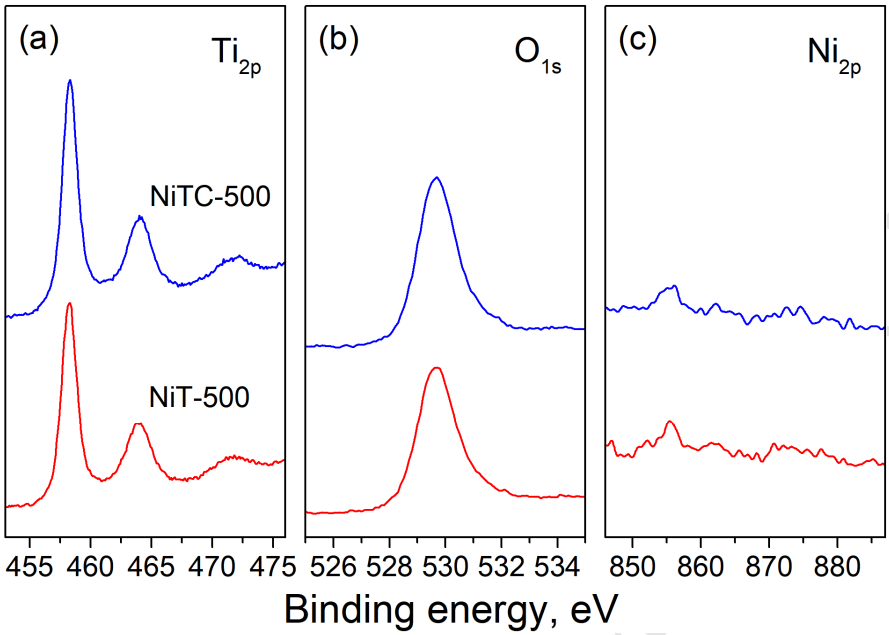

Figure 6.

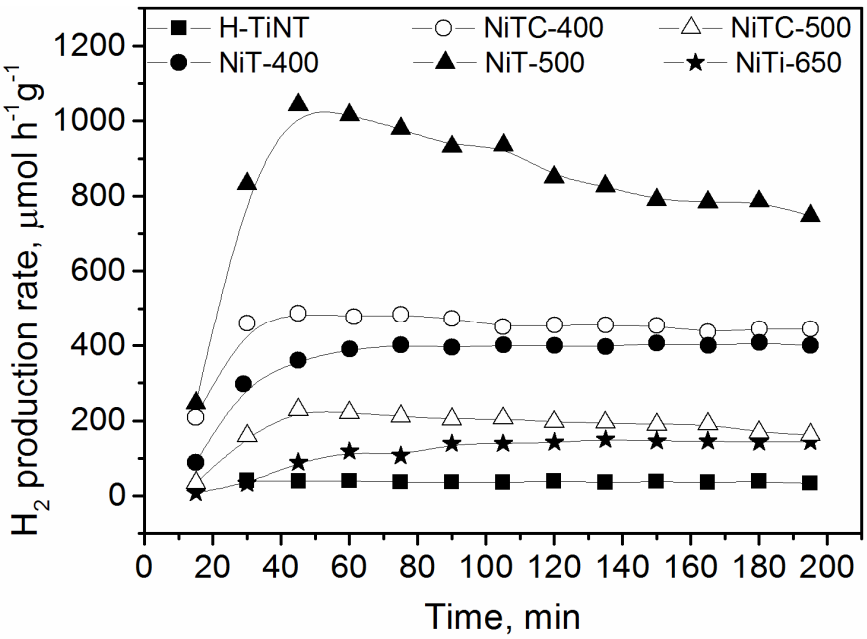

Figure 7.

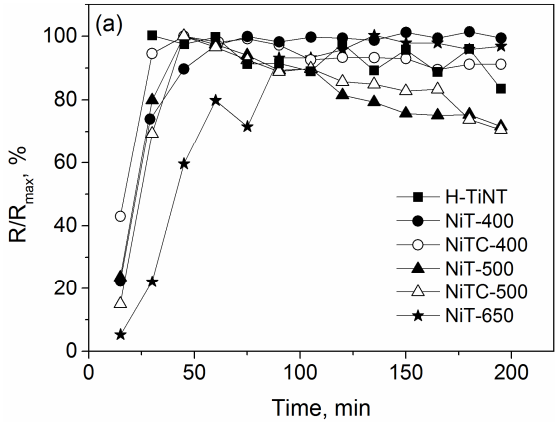
(a)
R/R$_{max}$, %
Time, min
H-TiNT
NiT-400
NiTC-400
NiT-500
NiTC-500
NiT-650

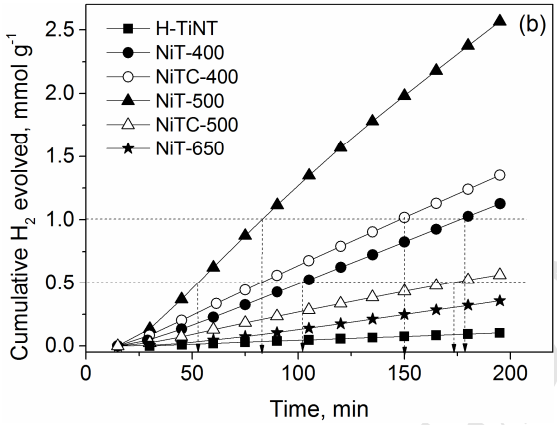
(b)
Cumulative H$_2$ evolved, mmol g^{-1}
Time, min
H-TiNT
NiT-400
NiTC-400
NiT-500
NiTC-500
NiT-650

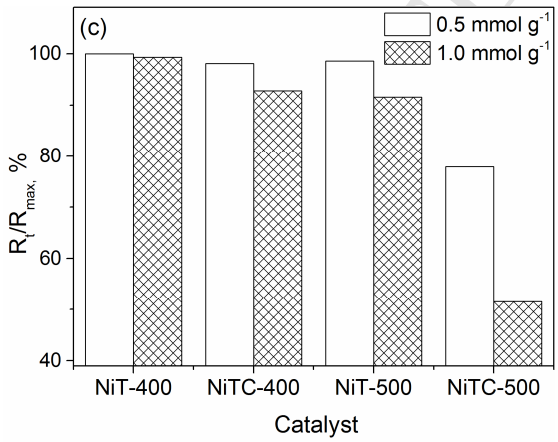
(c)
0.5 mmol g^{-1}
1.0 mmol g^{-1}
R$_t$/R$_{max,}$ %
NiT-400
NiTC-400
NiT-500
NiTC-500
Catalyst

Table 1. Elemental composition by EDX analysis, reduction properties and textural characteristic of H-TiNT and series of synthesized Ni-modified titanate/titania catalysts

Sample	H_2 consumed [a], μmol g^{-1}	Ni(0) content [b], wt %	EDX-Na, wt %	EDX-Ti, wt %	S_{BET} [c], $m^2 g^{-1}$	V_{total} [d], $cm^3 g^{-1}$	V_{meso} [e], $cm^3 g^{-1}$	D_p [f], nm
H-TiNT	-	-	-	70.5	283	1.19	0.82	13
NiT-400	40.3	0.2	n.d.	n.d.	201	1.09	0.73	15
NiTC-400	17.9	0.1	n.d.	n.d.	188	1.09	0.69	15
NiT-500	170.0	1.0	4.80	56.8	53	0.39	0.15	65
NiTC-500	145.4	0.9	5.30	52.4	34	0.33	0.09	60
NiT-650	281.1	1.6	6.82	54.8	25	0.10	0.05	70

[a] The amount of hydrogen experimentally consumed for the reduction of Ni(II) species at predetermined temperature, presented per mass of the catalyst,

[b] The content of the metallic nickel of the reduced catalyst based on the weight of the catalyst, calculated from the amount of hydrogen experimentally consumed,

[c] Specific surface area calculated using Brunauere Emmette Teller (BET) equation,

[d] Total pore volume (Gurvich) determined at a relative pressure $p/p_0 = 0.99$,

[e] Mesopore volume determined from the Barrete Joynere Halenda (BJH) method,

[f] Pore diameter with the highest pore volume in BJH adsorption isotherm,

n.d.: not determined.

Table 2. Maximal hydrogen production rates over H-TiNT and series of synthesized Ni-modified titanate/titania catalysts; experimental conditions: temperature 25 ºC, concentration of catalysts 0.5 mg mL^{-1}, concentration of 2-propanol 1.0 vol %

	H_2 production rate	
Sample	μmol h^{-1} g^{-1}	μmol h^{-1} m^{-2}
H-TiNT	40	0.14
NiT-400	404	2.01
NiTC-400	487	2.66
NiT-500	1042	19.7
NiTC-500	229	6.74
NiT-650	149	5.96

Supporting Information

Efficient photocatalytic hydrogen production over titanate/titania nanostructures modified with nickel

Jasmina Dostanić[a], Davor Lončarević[a], Vladimir B. Pavlović[b], Jelena Papan[c], Jovan M. Nedeljković[c]

[a]*Institute of Chemistry, Technology and Metallurgy, University of Belgrade (National Institute), Department of Catalysis and Chemical Engineering, Njegoševa 12, Belgrade, Republic of Serbia*

[b]*Faculty of Agriculture, University of Belgrade, Department of Agricultural Engineering, Nemanjina 6, 11080 Zemun, Republic of Serbia*

[c]*Institute of Nuclear Sciences Vinča, University of Belgrade, P.O. Box 522, 11001 Belgrade, Republic of Serbia*

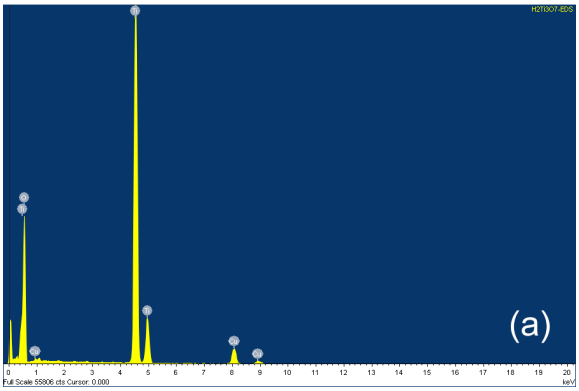

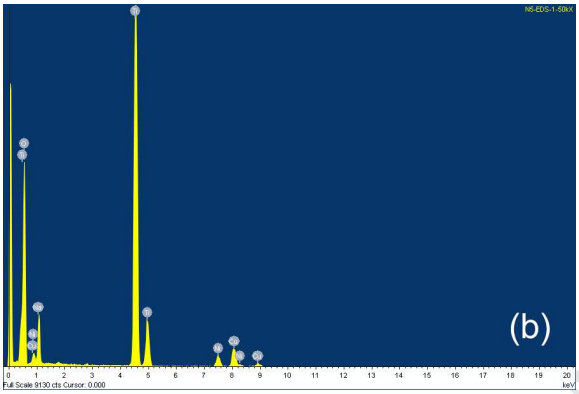

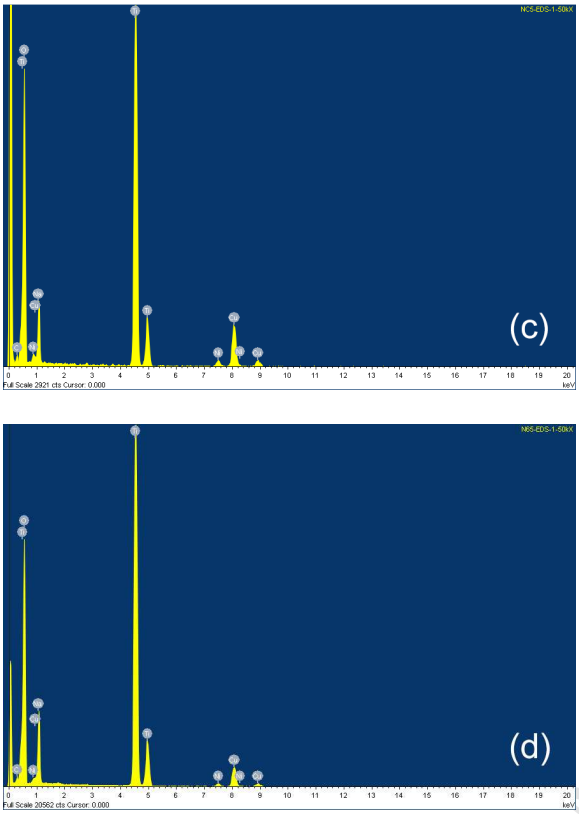

Figure S1. EDX spectra of **(a)** H-TiNT, **(b)** NiT-500, **(c)** NiTC-500 and **(d)** NiT-650.

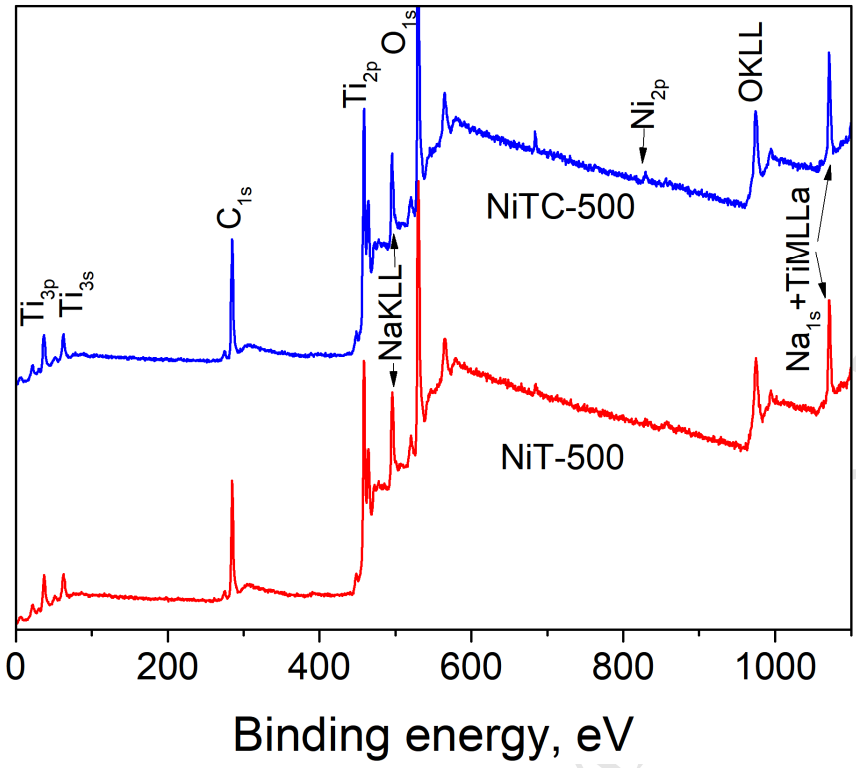

Figure S2. XPS survey spectrum of the prepared NiT-500 and NiTC-500.

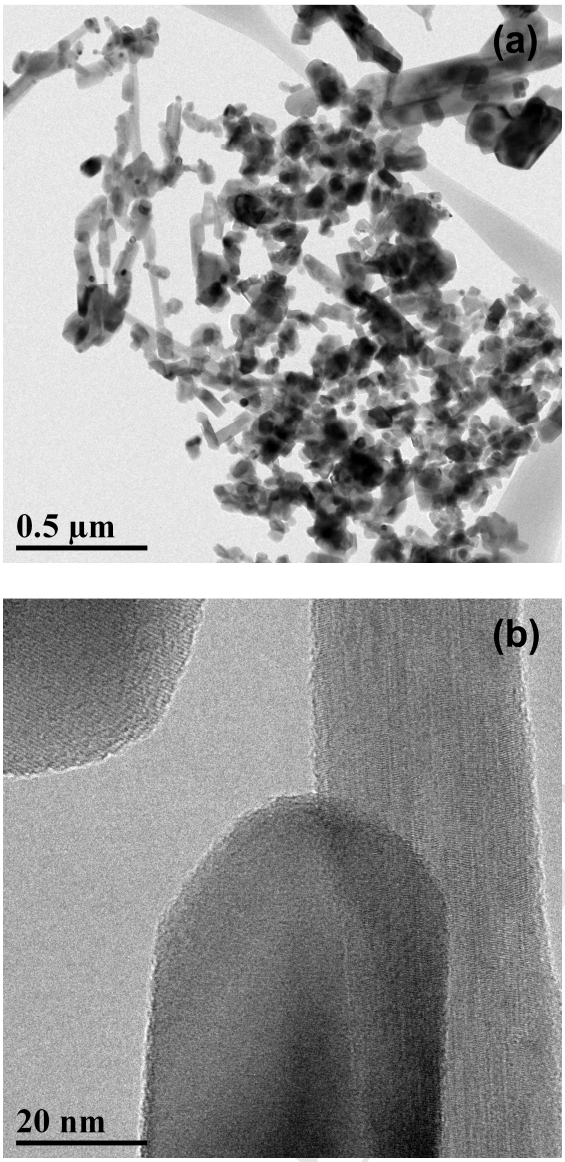

Figure S3. (a) Low- and **(b)** high-magnification TEM images of the prepared NiT-650.

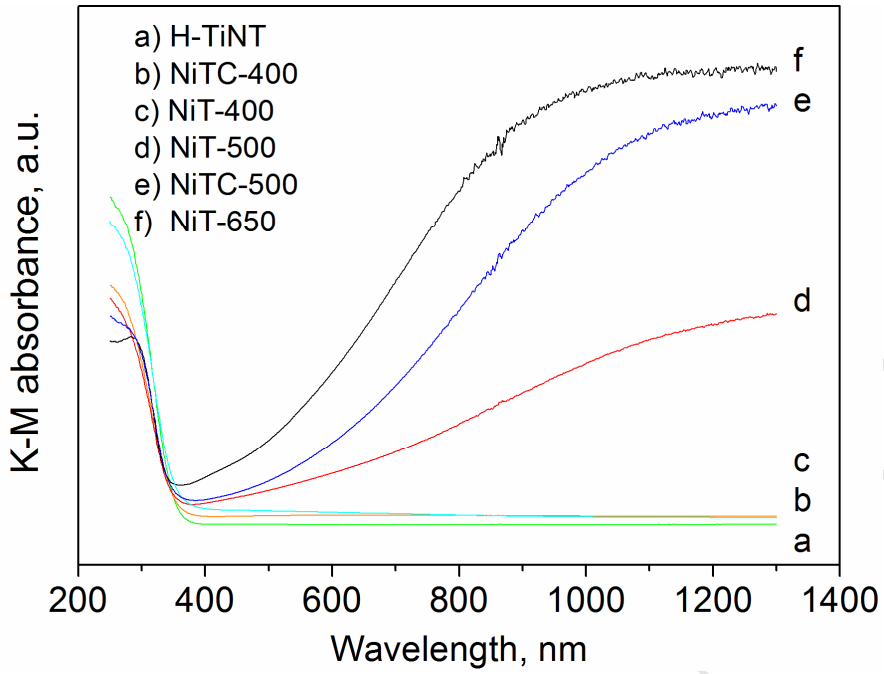

Figure S4. Kubelka-Munk transformations of diffuse reflection data of H-TiNT and series of synthesised Ni-modified titanate/titania catalysts.